Earth Planet. Sci. Lett. 687 (2026) 120060

Contents lists available at ScienceDirect

Earth and Planetary Science Letters

journal homepage: www.elsevier.com/locate/epsl

Earthquake nucleation in the laboratory: Insights from space-time imaging of quasi-static precursory slip under tri-axial conditions

P. Dublanchet[a,*], F.X. Passelégue[b], H. Chauris[a,c], A. Gesret[a], C. Noël[b]

[a] Mines Paris, PSL University Center for Geosciences, Fontainebleau, 77300, France
[b] Université Côte d'Azur, CNRS, Observatoire de la Côte d'Azur, IRD, Géoazur, Sophia Antipolis, 06560, France
[c] Mines Paris, PSL University STIM, Fontainebleau, 77300, France

A R T I C L E I N F O

Editor: J.P. Avouac

Keywords:
Earthquake nucleation
Aseismic slip
Critical nucleation length
Rupture front
Tri-axial loading
Saw-cut sample
Friction

A B S T R A C T

We investigate the nucleation of frictional instabilities in Westerly granite using a triaxial apparatus reproducing stress conditions equivalent to depths of up to ∼3 km. By inverting local axial strain measurements, we reconstruct the space-time evolution of aseismic preslip preceding 21 laboratory stick-slip events. Nucleation initiates on a localized patch and expands quasi-statically at rates of 10–50 m day^{-1} until dynamic rupture occurs, most commonly when the slipping zone reaches the fault boundaries. Across successive fault reactivations, the nucleation behavior evolves systematically with cumulative slip: the expansion rate decreases, the nucleation duration increases from ∼5 s to ∼30 s, and the effective nucleation length grows until it approaches the fault size. These changes cannot be explained solely by variations in normal stress and instead reflect irreversible modifications of frictional properties induced by slip accumulation. We interpret this evolution as the mechanical signature of possible progressive wear, gouge production, and or local melting occurring along the interface, leading to an increase by a factor of ∼3 in the critical slip distance governing frictional weakening. Our results provide direct experimental evidence that earthquake nucleation is not controlled by constant frictional parameters but evolves with fault history. They highlight the importance of cumulative slip and fault memory in governing the transition from stable to unstable slip under seismogenic stress conditions.

1. Introduction

Earthquakes are commonly interpreted as frictional instabilities developing on critically stressed crustal faults (Ohnaka and Shen, 1999). Their initiation, referred to as *nucleation*, may manifest on natural faults either as accelerating aseismic slip transients (Roeloffs, 2006; Ruiz et al., 2014; Uchida and Matsuzawa, 2013; Nagao et al., 2014; Bletery and Nocquet, 2023) or as foreshock sequences (Dodge et al., 1996; Bouchon et al., 2013; Cabrera et al., 2022). Determining the physical mechanisms that govern this transition from stable to dynamic slip is therefore central to understanding earthquake triggering and to improving physics-based approaches to earthquake hazard assessment (Dieterich, 1978).

Direct observations of aseismic nucleation on natural faults are limited by the spatial resolution of geodetic networks and by the lack of stress information at seismogenic depths. Laboratory experiments overcome these limitations by reproducing stick-slip instabilities on centimetric to metric faults under controlled stress conditions. Two-dimensional (2D) setups, such as direct-shear apparatus, have been widely used to monitor fault reactivation either through distributed slip sensors (McLaskey and Kilgore, 2013; Selvadurai and Glaser, 2017) or through photoelastic imaging using transparent analog materials such as PMMA (Nielsen et al., 2010; Latour et al., 2013; Guérin-Marthe et al., 2019a; Gvirtzman and Fineberg, 2021; Gvirtzman et al., 2025). In such large-scale 2D experiments, normal stresses rarely exceed 20 MPa. Detailed 2D observations further show that nucleation begins as a quasi-static, localized slip patch that expands progressively before transitioning to an accelerating phase leading to dynamic failure (Ohnaka and Shen, 1999; Nielsen et al., 2010; Latour et al., 2013; Guérin-Marthe et al., 2019b).

Stress levels representative of seismogenic depths (up to ∼100 MPa) can be achieved in triaxial apparatus using centimetric rock samples (McLaskey and Lockner, 2014; Passelègue et al., 2017; Dresen et al., 2020; Marty et al., 2023; Wang and Dresen, 2025). In these configurations, the approach to stick-slip failure is generally tracked with strain-gauge arrays and acoustic emission sensors. Such studies consistently reveal a precursory phase of accelerating aseismic slip preceding dynamic rupture, often accompanied by clusters of acoustic emissions in-

* Corresponding author.
E-mail addresses: pierre.dublanchet@mines-paristech.fr (P. Dublanchet), Francois.PASSELEGUE@geoazur.unice.fr (F.X. Passelégue), herve.chauris@minesparis.psl.eu (H. Chauris), alexandrine.gesret@minesparis.psl.eu (A. Gesret), corentin.noel@geoazur.unice.fr (C. Noël).

https://doi.org/10.1016/j.epsl.2026.120060
Received 10 June 2025; Received in revised form 20 February 2026; Accepted 20 April 2026
Available online 6 May 2026

terpreted as laboratory foreshocks (McLaskey and Lockner, 2014; Passelègue et al., 2017; Dresen et al., 2020; Marty et al., 2023; Wang and Dresen, 2025).

The transition to dynamic propagation occurs when the preslip zone reaches a critical length, L_c, which depends at the first order on the normal stress σ_n and the frictional properties of the interface (Dieterich and Linker, 1992; He et al., 1998; Chambon and Rudnicki, 2001; Latour et al., 2013; Leeman et al., 2018; Bedford and Faulkner, 2021; Giorgetti and Violay, 2021). This dependence on the normal stress is captured by slip-weakening and rate-and-state friction theories (Uenishi and Rice, 2003; Rubin and Ampuero, 2005), assuming frictional properties remain constant during loading. In practice, however, stability transitions have also been observed on laboratory faults with increasing cumulative shear displacement, wear, gouge formation (Dieterich, 1981; Biegel et al., 1989; Marone et al., 1990, 1992; Marone and Kilgore, 1993; Beeler et al., 1996; Mair and Marone, 1999; Rathbun and Marone, 2010; Hadizadeh et al., 2015; Scuderi et al., 2017b; Shreedharan et al., 2020; Noël et al., 2023), loading rate (Kato et al., 1992; Marone, 1998; Mclaskey and Yamashita, 2017; Xu et al., 2018; Leeman et al., 2018; Guérin-Marthe et al., 2019a, 2023; Wang and Dresen, 2025), temperature (Blanpied et al., 1998), fluid pressure changes (Scuderi et al., 2017a; Noël et al., 2019), fault material heterogeneity (Arts et al., 2024; Bedford et al., 2022), roughness (Harbord et al., 2017; Dresen et al., 2020; Fryer et al., 2022; Guérin-Marthe et al., 2023), fabric evolution (Pozzi et al., 2022) or fault geometry (Gvirtzman et al., 2025). Stability transitions in such experiments can generally be attributed to non-constant frictional parameters, i.e. rate-and-state parameters $a - b$ and d_c that are not material/interface properties but rather evolve with slip accumulated on faults leading to progressive wear and microstructural evolution. These effects can be enhanced under high confining pressures typical of triaxial conditions (Wang and Dresen, 2025). However, it remains unclear whether such slip-induced evolution of frictional properties translates into measurable changes in nucleation behavior. In particular, the optical imaging techniques that have enabled detailed observations of nucleation in transparent materials cannot be applied to opaque rock samples subjected to high confining pressures. As a result, the spatio-temporal evolution of preslip under truly seismogenic stress conditions remains largely unconstrained.

To address this gap, we recently developed a kinematic inversion method to reconstruct quasi-static slip along faults loaded in triaxial configurations using local strain measurements (Dublanchet et al., 2024). A first application, conducted on granite at 90 MPa confining pressure, revealed a quasi-static slip episode lasting about 20 s, accumulating several micrometers of slip, and expanding at rates of 100–200 m day^{-1} (Dublanchet et al., 2024), closely resembling the early quasi-static stage of nucleation observed in 2D setups. Here, we extend this approach to a larger dataset comprising 31 stick-slip events in Westerly granite under confining pressures between 30 and 90 MPa. By imaging the spatio-temporal evolution of precursory slip for the 21 best-recorded events, we quantify how the nucleation process evolves with cumulative fault slip and investigate how wear-related frictional changes control the transition from stable to unstable slip.

2. Data and precursory slip imaging

2.1. Data

In the following we analyze the nucleation of 21 among 31 stick-slip events triggered by tri-axial loading of a cylindrical Westerly granite saw cut sample (Fig. 1). The experiment is presented in details in Dublanchet et al. (2024). Here we provide a brief summary of the experimental conditions.

The sample is 8.8 cm long and has a diameter of 4 cm. It consists of Westerly granite made of 35 % K-feldspar, 31 % plagioclase, 28 % quartz and 6 % phylosilicate (Chayes, 1950), with Youngs modulus $E = 75$ GPa and Poisson ratio $\nu = 0.25$. The fault surface, oriented at 30° from the principal stress σ_1, has been polished before loading with a silicon carbide powder (#1200 grit) to approximately achieve a 5 μm roughness. For a given confining pressure $P_c = \sigma_3$, σ_1 is increased by imposing a constant volume injection rate in the axial chamber. This injection rate is maintained constant throughout the entire experiment, including during stick-slip events, so that fault instabilities occur under continuous loading conditions. The resulting shortening rate imposed by axial chamber injection is $1.5 \mu\text{m.s}^{-1}$. This procedure is repeated at different levels of increasing (30, 60 and 90 MPa) and decreasing (60 MPa, 30 MPa) confining pressures to explore different levels of normal stress on the fault. Three gap sensors located outside the loading vessel continuously measured the shortening of the whole column (sample and apparatus) during the experiment. This data combined with differential stress measurements is used to estimate the sample elastic shortening, and the cumulative macroscopic slip occurring on the fault sample, as detailed in Dublanchet et al. (2024). All the measurements were done at a 2400 Hz sampling rate.

The evolution of confining pressure, shear stress, normal stress and cumulative fault slip are shown in Fig. 1a. Step-like increases in fault slip and associated shear stress drops mark the occurrence of macroscopic slip events (SEs). At each tested confining pressure, the peak shear stress leading to instability increases slightly with cumulative fault displacement, suggesting a progressive strengthening of the interface, as observed in previous studies (Passelègue et al., 2016). This trend is expressed as a gradual rise in the effective static friction coefficient f_0 across successive fault reactivations (Figure S1a). Overall, f_0 remains approximately constant during the first two confining levels (30 and 60 MPa), before increasing from about 0.35 to 0.55 at higher confinement (Figure S1a). This apparent strengthening of f_0 may reflect the limited cumulative slip at each stage, which prevents the fault from reaching steady-state friction, as previously reported by Richardson and Marone (1999). The coseismic stress drops associated with individual SEs range from 2 to 18 MPa, corresponding to fault slips of 40–150 μm (Figure S1b).

As shown in Fig. 1b, slip events are all preceded by micrometric precursory slip accumulation on the fault. This preslip stage is hereafter considered as the nucleation phase.

In addition, an array of 8 strain gauges (G1 to G8) allowed to measure the axial strain ε_{11} at different locations of the sample, and as close to the fault as possible (2.4 mm below it). Here again, axial strain was acquired at 2400 Hz. The position of the gauges is the same as in Dublanchet et al. (2024), and is reported in Fig. 2f, S2 to S43 of the supplementary material. In between two SE, the sample experiences both an elastic and an inelastic strain, assumed to result from bulk response and transient fault slip respectively. To extract the inelastic component of strain, we removed the linear trend associated with the elastic response, as detailed in Dublanchet et al. (2024). Examples of resulting inelastic strain arising from nucleation pre-slip are shown in Fig. 2a-e.

2.2. Kinematic inversion of precursory slip

We use the kinematic inversion scheme developed by Dublanchet et al. (2024) to infer from inelastic strain measurements (Fig. 2a-e) the spatio-temporal evolution of preslip on the fault during SE nucleation. Here we recall the main features of the method, additional details about the parametrization are provided in the supplementary material.

The fault surface is discretized using triangular elements, and the fault slip at each node (24 in total) is parametrized as a cosine ramp function of finite duration and amplitude. The duration of the ramp is not limited to the nucleation duration so that our parametrization is able to capture unstable accelerating slip. The inversion scheme allows to retrieve the three parameters (onset time of slip, ramp duration, and slip amplitude) at each node that minimize the squared difference between observed and computed strains at the strain gauge locations, as well as between the observed and computed averaged slip on the fault. In order to compute the strains resulting from a given fault slip distribution, we

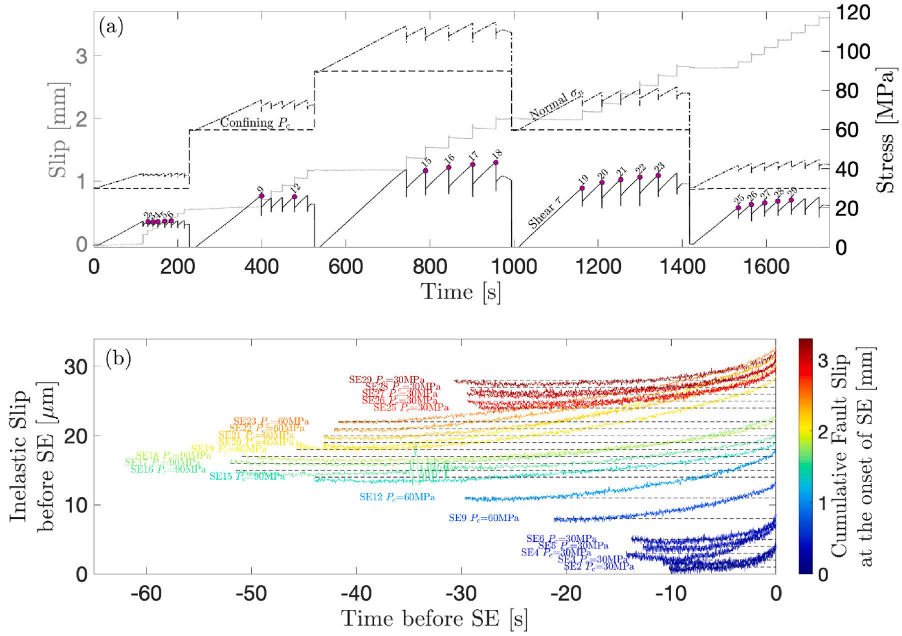

Fig. 1. Evolution of the shear stress (solid black), confining stress P_c (dashed black), normal stress σ_n (dashed dotted black) and cumulative fault slip δ (solid gray) during stick-slip experiments. Purple dots indicate the timing of macroscopic slip events (SEs) used in this study. (b) Evolution of the fault slip measured macroscopically prior the instabilities, for SEs indicated in (a). Colors refers to the cumulative fault slip at the onset of each SEs. For clarity, time series are vertically offset by 2 μm for each SE occurring in the experiment. Horizontal dashed black lines indicate the 0 of the different time series.

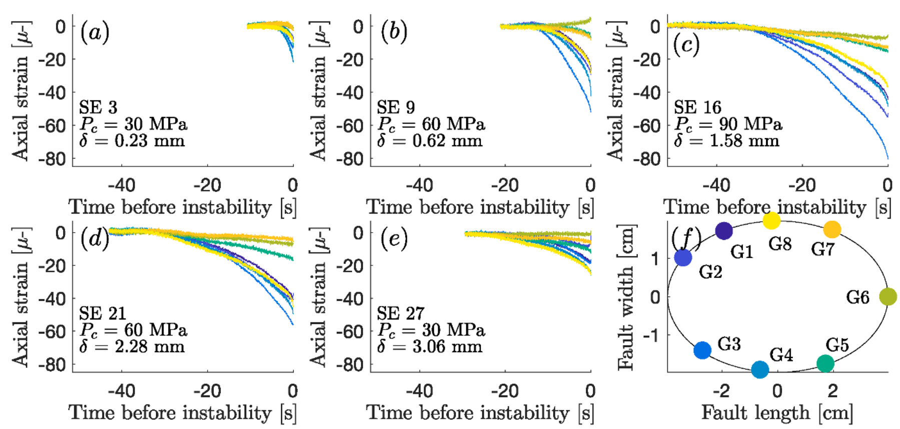

Fig. 2. Evolution of axial strain before 3 SEs occuring under 30 (a), 60 (b) and 90 (c) MPa confining pressure, and decreasing back the confining pressure to 60 (d) and 30 (e) MPa. One SE per level of confining is shown here. The colored lines correspond to the strain gauges location in panel (f). SE ID, confining and cumulative slip at the onset of each SE δ are indicated in the right bottom corner of the panels.

use a set of elasto-static Green's functions precomputed using a finite elements approach. In doing so, we assume the granite is a homogeneous isotropic elastic medium with Young's modulus E = 75 GPa and Poisson ratio $\nu = 0.25$ as obtained from the measure of the elastic response of the sample. We also consider the real cylindrical geometry of the sample and the experimental loading as boundary conditions.

For each slip event, we first perform a deterministic optimization step relying on L-BFGS-B algorithm (Broyden, 1970; Fletcher, 1970; Goldfarb, 1970; Shanno, 1970), that converges to a minimum of the cost function (squared difference between modeled and observed strains and slip). Following the synthetic tests presented in Dublanchet et al. (2024), we use at this step a regularization of the cost function aiming at minimizing the gradient norm of the parameters. Based on the synthetic tests of Dublanchet et al. (2024) conducted with a similar setup, the regularization parameter λ we consider here is $\lambda = 0.1$. The deterministic step allows to image slip events with a typical size of about 4 mm, with an uncertainty of about 4 μm, as discussed in (Dublanchet et al., 2024). The resulting best model is used in a second step as an initial model for a global Bayesian exploration carried out with a MCMC algorithm (Metropolis et al., 1953; Hastings, 1970). For each accepted model in the MCMC chain, we reconstruct the slip history of each node, so as to assess the uncertainty on the spatio-temporal evolution of fault slip during nucleation.

The cost function to be minimized during the deterministic optimization and MCMC explorations assumes diagonal covariance matrices, where diagonal elements are computed from the standard deviation of the observed strain and mean slip, i.e. 10^{-6} and $0.1\mu m$ respectively. These values are readjusted before starting optimization iterations to account for the epistemic uncertainty and for the quality of the strain gauges, estimated by their ability to capture the elastic strain of the sample. All details are provided in Dublanchet et al. (2024).

To ensure convergence of the MCMC, here again we followed the conclusions of Dublanchet et al. (2024), and performed for each SE 10^8 exploration iterations. In general, we achieved an acceptance rate be-

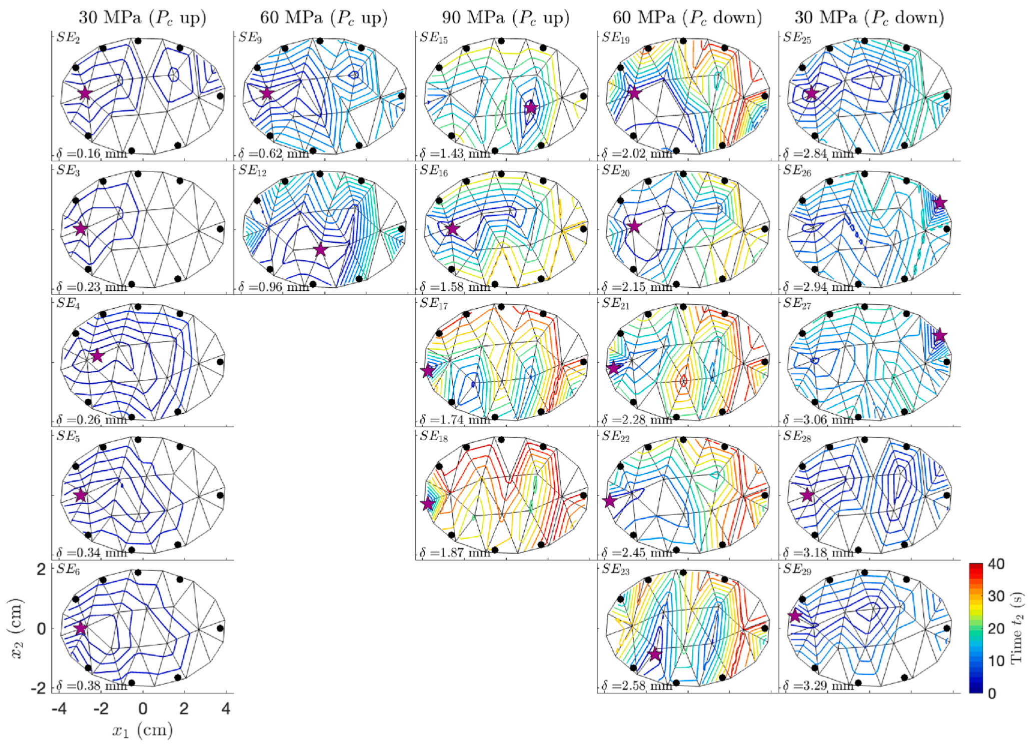

Fig. 3. Rupture time t_2, indicating the extent of nucleation patch. Subscript 2 refers to the slip threshold used to track the nucleation zone: each contour encloses regions of the fault that have experienced more than 2 μm at the time indicated by the color scale. t_2 is computed from the mean reconstructed slip history. Panels show a top view of the fault. x_1 and x_2 are the coordinates in the fault plane. Slip occurs in the positive x_1 direction. The grid used for the inversion of slip history is shown with solid black lines. Black dots indicate strain gauges position. The magenta star indicates the first node to slip. Cumulative fault slip δ at the onset of SEs is indicate in each panel.

tween 0.2 and 0.3. We could however achieve convergence and a satisfactory fit to the observations only for 21 of the 31 SE, shown with purple dots in Fig. 1a (Figures S45 to S65 of the supplementary material). The 21 SE nevertheless cover the whole range of increasing and decreasing confining pressures.

3. Results

A summary of the space-time evolution of fault slip inferred during the nucleation of 21 SEs is shown in Fig. 3. The detailed histories of fault slip and slip rate are presented in Figures S2 to S43 of the supplementary material. We represent the mean reconstructed slip history, corresponding to the average prediction of all models accepted during the MCMC exploration phase. The contours shown in Fig. 3 highlight the rupture time t_2, the subscript 2 referring to the slip threshold used to track the nucleation zone. Each contour of t_2 encloses regions of the fault that have experienced more than 2 μm of slip at the time indicated by the color scale. Note that t_2 is computed from the onset of nucleation, with $t_2 = 0$ when the first point on the fault accumulates more than 2 μm of slip. In all cases, nucleation is initiated on a small patch of the fault (hereafter referred to as the nucleation site). The slipping patch then expands in all directions until macroscopic failure (or SE) occurs. For some slip events, we observe a secondary nucleation patch: SE_2 ($P_c = 30$ MPa, $\delta = 0.16$ mm of cumulative fault slip), SE_9 ($P_c = 60$ MPa, $\delta = 0.62$ mm), SE_{15} and SE_{17} ($P_c = 90$ MPa, $\delta = 1.43$ and 1.74 mm), SE_{21} and SE_{23} ($P_c = 60$ MPa, $\delta = 2.28$ and 2.58 mm), and all SEs for $P_c = 30$ MPa with $\delta > 2.8$ mm. In each case, the total accumulated slip is on the order of 5–30 μm, and slip rates range from 0.1 to 5 μm s^{-1} (Figures S2 to S43). Note that not all nucleation patches reach the fault boundary at the time of macroscopic failure (SE onset), particularly for the first slip events of the ascending confining stage at $P_c = 30$ MPa and cumulative fault slip less than 0.38 mm. This feature will be discussed further below.

Fig. 3 also indicates the nucleation site (star) corresponding to the mean reconstructed slip. To account for the uncertainty in slip history, we examined how the nucleation sites vary across the full range of models accepted during the MCMC exploration. The results are shown in Fig. 4c. Most SEs nucleate in the central left part of the fault (near $x_1 = -2$ cm, $x_2 = 0$ cm), particularly when the cumulative fault slip is less than 2.5 mm. Exceptions occur for SEs triggered after 2.5 mm of cumulative slip, at $P_c = 30$ MPa during the decreasing confinement stage, which tend to nucleate preferentially on the right side of the fault ($x_1 > 0$). This shift likely reflects an evolution of the interface properties with cumulative slip and repeated failures, consistent with the increase in effective static friction coefficient shown in Figure S1a. In any case, the results in Fig. 4a indicate that the nucleation site cannot be located with a precision better than a few centimeters.

To further characterize the nucleation process, we computed the temporal evolution of the nucleation patch area, S_{nuc}, up to the onset of macroscopic failure (SE). We define $S_{nuc}(t)$ as the total fault area that has accumulated more than a threshold slip $u_{th} = 2$ μm at time t. This quantity was computed for all reconstructed slip histories lying within one standard deviation (1σ) of the mean slip distribution shown in Fig. 3 and Figures S2– S43. Recall that the MCMC exploration yields a suite of models, each providing a possible slip history for every fault node. The resulting $S_{nuc}(t)$ is plotted in Fig. 4b as a function of cumulative fault slip at SE onset, while the corresponding rate of surface expansion is shown in Fig. 4c.

For all SEs, the rate of nucleation zone expansion, $\dot{S}_{nuc}$, first increases and then decreases as the slip fronts approach the fault boundaries ($S_{nuc} = S_f$; Fig. 4c). Throughout the entire nucleation phase, expansion rates remain below 10^{-3} m^2 s^{-1}. The results shown in these figures indicate that the behavior of the nucleation zone evolves systematically

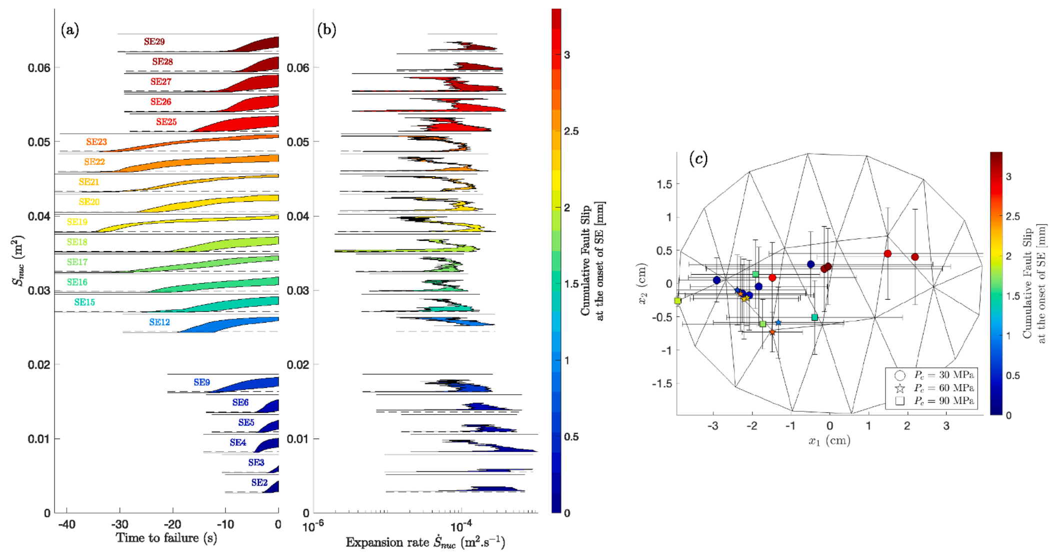

Fig. 4. (a): Nucleation zone surface S_{nuc} expansion before macroscopic failure for all the SEs analyzed in the experiment. The shaded area between two black lines indicates the 1σ range of predictions of the accepted models during the MCMC exploration. The black dashed lines indicates the resolution of the inversion method (surface S_0), and the solid black line indicates the total experimental fault surface (surface S_f). Colors refer to the cumulative fault slip at the onset of SEs. Results are vertically offset by $1.1S_f$ for each SE occurring in the experiment for clarity. (b): Rate of nucleation zone surface expansion $\dot{S}_{nuc}$ for all the SE analyzed in the experiment. Rates are represented as a function of the nucleation zone surface S_{nuc}. As in (a), results are vertically offset, and dashed and solid black lines indicate S_0 and S_f. (c): Nucleation site of SEs (fault location where slip first exceeds 2 μm). Triangular mesh used for the inversion is shown with thin solid black lines. Symbols indicate the mean nucleation site determined from the reconstructed slip histories of all the models accepted in the MCMC exploration. Error bars indicate the one standard deviation on nucleation site position. Symbols are color-coded with the cumulative fault slip at the onset of SEs.

with the accumulation of stick-slip events on the fault, again suggesting a non-recoverable evolution of the interface properties.

Fig. 5a and c show the variations in expansion rate $\dot{S}_{\text{nuc}}$ and nucleation duration t_n as a function of cumulative fault slip. The value of $\dot{S}_{\text{nuc}}$ reported here corresponds to the average expansion rate before deceleration, which typically occurs when S_{nuc} exceeds $0.3S_f$, where S_f is the total available fault surface (Fig. 4b). The nucleation duration t_n is defined as the time interval between $S_{\text{nuc}} > S_0$ (where S_0 is the minimum resolvable area derived in Dublanchet et al., 2024) and the onset of the SE.

As cumulative slip increases, the average expansion rate decreases (Fig. 5a) while the nucleation duration increases (Fig. 5c). The first events at $P_c = 30$ MPa nucleate within approximately 5 s, whereas later events, after about 2 mm of accumulated slip, require up to 30 s to nucleate, irrespective of confining pressure. Consistently, the expansion rate decreases from 20 to 40 m^2 day^{-1} to 3–5 m^2 day^{-1} over the same range of cumulative slip. During the final stage of decreasing P_c, additional slip accumulation results in the nucleation duration shortening again to about 10 s, although the initial 5 s duration is not recovered. Similarly, the expansion rate slightly increases to 10–20 m^2 day^{-1} after 1 mm of cumulative slip, but the rapid expansion observed during the earliest events is not reproduced. Overall, the variations in expansion rate and nucleation duration are asymmetric with respect to P_c evolution, indicating that the changes in nucleation behavior cannot be explained solely by confining pressure. The cumulative slip must also be considered.

Fig. 5b further shows that $\dot{S}_{\text{nuc}}$ approximately scales with the maximum slip rate V_s, except for one event recorded during the decreasing confinement stage at $P_c = 60$ MPa. The surface expansion rate $\dot{S}_{\text{nuc}}$ of the pre-slip patch can be approximately related to the rupture propagation speed and the maximum slip rate, assuming that the pre-slip zone behaves as a circular crack of radius R_{nuc}, such that:

$$\dot{S}_{nuc} = 2\pi R_{nuc}\dot{R}_{nuc} = 2\pi R_{nuc}\frac{G}{\Delta\tau_n}V_s, \tag{1}$$

where G is the shear modulus of the granite, and $\Delta\tau_n$ is the static stress drop driving nucleation. In writing the second equality in Eq. (1), we applied a simple fracture-mechanics scaling (Lawn, 1993) to relate the rupture speed $\dot{R}_{\text{nuc}}$ to the slip rate V_s. The expansion rates $\dot{S}_{nuc}$ shown in Fig. 5b are average expansion rates for $S_{nuc} < 0.3S_f$, and therefore should follow scaling (1), with $R_{nuc} = 2\sqrt{0.3S_f/\pi}/3$. Note that this provides only a first-order approximation, given the complex slip patterns shown in Fig. 3. Nevertheless, as illustrated in Fig. 5b, it reproduces the general trend obtained from our inversions, with $\Delta\tau_n$ values ranging between 5 and 20 MPa. The outlier corresponds to SE_5 during the decreasing confinement stage at $P_c = 60$ MPa. As shown in the slip and slip-rate maps of the supplementary material, the inversion selected models in which a single node accommodates nearly all the slip, within a region that is likely poorly resolved. This may explain the anomalously small expansion rate and suggests that the MCMC exploration did not sufficiently sample the parameter space in this case. Considering the uncertainties in slip rate and rupture speed, we cannot resolve any significant variation in $\Delta\tau_n$ across successive fault reactivations.

We also compute an effective nucleation length from the surface expansion as:

$$L_c^* = \sqrt{S_{nuc,f}}, \tag{2}$$

where $S_{nuc,f}$ is the final value of the nucleation patch surface, i.e. at the onset of the SE. The effective nucleation length L_c^* is shown in Fig. 5d. The first series of slip events (SEs) at 30 MPa are characterized by L_c^* values significantly smaller than the fault length. In contrast, subsequent SEs involve nucleation patches that expand to the fault boundaries, resulting in L_c^* values approaching the characteristic fault length, here estimated as $\sqrt{S_f}$. This transition occurs once the fault has accumulated more than ∼1 mm of slip, consistent with the rupture-front evolution shown in Fig. 3. Notably, even after reducing the confining pressure back to 30 MPa, L_c^* remains close to the fault length, indicating that the change in nucleation behavior is not reversible upon unloading. We also indicate in Fig. 5d the expected nucleation length evolution assuming a pure normal stress dependence (black line). For that we use the theoretical scaling of the critical nucleation length with inverse normal stress

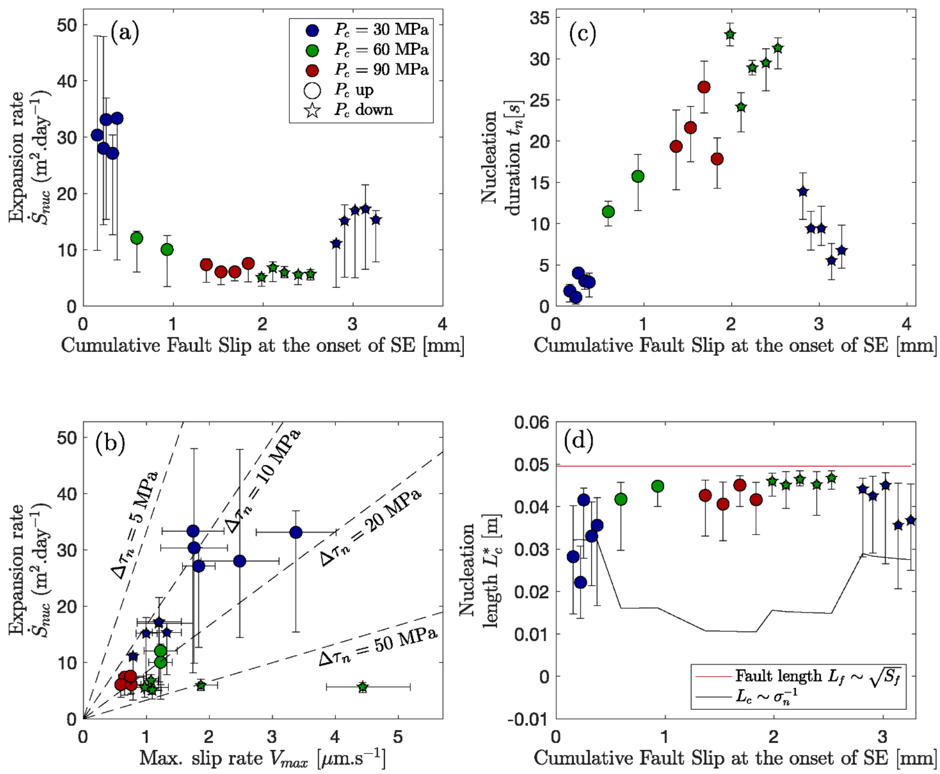

Fig. 5. (a) Average rate of expansion of the nucleation zone, computed from results of Fig. 4 for $S_0 < S_{nuc} < 0.3S_f$. Error bars indicate the 1σ range of model predictions (shaded areas in Fig. 4). (b) Scaling between expansion rate and maximum slip rate on the fault. Dots are inversion results. Black dashed lines indicate the scaling of Eq. (1) with different values of the nucleation stress drop $\Delta\tau_n$ and $R_{nuc} = 2\sqrt{0.3S_f/\pi}/3$.(c) Nucleation duration (defined as the time interval where $S_f > S_{nuc} > S_0$) of SEs. (d) Effective nucleation length L_c^* of SEs. Dots are inversion results. The red dashed line indicates the effective fault length L_f computed as $\sqrt{S_f}$. The black line indicate the expected nucleation length change under pure inverse normal stress σ_n dependence, according to Eq. (2).

σ_n of the form:

$$L_c^* = \frac{\xi}{\sigma_n} = \frac{Gd_c}{\sigma_n}F. \quad (3)$$

Scaling (3) has been established for both slip-weakening friction (Campillo and Ionescu, 1997; Uenishi and Rice, 2003) and rate-and-state friction (Rubin and Ampuero, 2005), and has been supported by previous laboratory observations (Latour et al., 2013). The factor ξ incorporates the shear modulus G, the critical slip distance d_c governing frictional weakening, and a functional dependence on additional friction parameters F. For slip-weakening friction, $F = 1/(f_0 - f_d)$, where f_0 and f_d denote the static and dynamic friction coefficients, respectively. For rate-and-state friction, F depends on the constitutive parameters a (direct effect) and b (state evolution) (Rubin and Ampuero, 2005). In our analysis, we calibrate the parameter ξ such that Eq. (3) reproduces the value of L_c inferred for the first SEs at 30 MPa confining pressure. The normal stress σ_n during the nucleation of subsequent SEs is directly determined from the measured axial and confining stresses. The resulting theoretical prediction deviates from the nucleation lengths obtained by slip inversion. This discrepancy indicates that the critical nucleation length does not obey a simple inverse dependence on σ_n with constant frictional parameters (d_c, f_0, f_d, or a and b). Instead, as slip events accumulate, L_c^* progressively increases and may exceed the experimental fault length. Such an increase cannot be captured by our measurements, as L_c^* is, by construction, bounded above by $\sqrt{S_f}$, the characteristic length of the experimental fault.

The occurrence of a SE even when L_c^* exceeds the fault length, rather than resulting in stable aseismic slip, can be understood from the evolution of shear stress during nucleation. To quantify this effect, we estimate the shear stress change τ induced by preslip from the strain-gauge measurements ε_δ (corrected for the linear elastic response of the sample) shown in Fig. 2, as

$$\tau = E\,\bar{\varepsilon}_\delta\,\frac{\sin 2\theta}{2}, \quad (4)$$

where E is the Young's modulus of the rock sample, $\bar{\varepsilon}_\delta$ is the inelastic axial strain averaged over the eight gauges, and $\theta = 30°$ is the angle between the fault plane and the axial direction. We then define an effective stiffness k as the average value of $-\partial\tau/\partial\delta$ during the nucleation phase. Fig. 6 shows the resulting values of k normalized by the normal stress σ_n (colored symbols), together with the normalized unloading stiffness k_u/σ_n (black dashed line). The unloading stiffness k_u is inferred from the coseismic response of the system, i.e., from the ratio between coseismic stress drop and coseismic slip (Figure S2). For a given SE (corresponding to a specific cumulative slip value in Fig. 6), we observe a sharp transition from k/σ_n (colored symbol) to k_u/σ_n (black dashed line) at the end of nucleation. Because σ_n remains approximately constant during this phase, this transition reflects a sudden drop of the effective stiffness from k to k_u. As detailed in the supplementary material, this drop marks the onset of rigid-block motion, which occurs once the preslip fronts reach the fault boundaries.

While the nucleation patch remains smaller than the available fault area, the effective stiffness scales approximately as $k \sim E^*/R_{nuc}$, where E^* is an effective elastic modulus accounting for both sample and apparatus compliance (see Supplementary Material), and R_{nuc} is the characteristic size of the slipping patch. Once the slipping zone reaches the fault boundaries, the two halves of the sample behave as rigid blocks sliding past one another. In this regime, k saturates at the constant unloading stiffness k_u, which controls the subsequent coseismic slip and stress drop. Unstable slip will thus occur if the rate of shear stress decrease (effective stiffness) becomes lower than the critical stiffness k_c, imposed by normal stress and frictional properties (according to scaling 3, $k_c \sim \sigma_n/Fd_c$). Observing SEs rather than aseismic slip means that

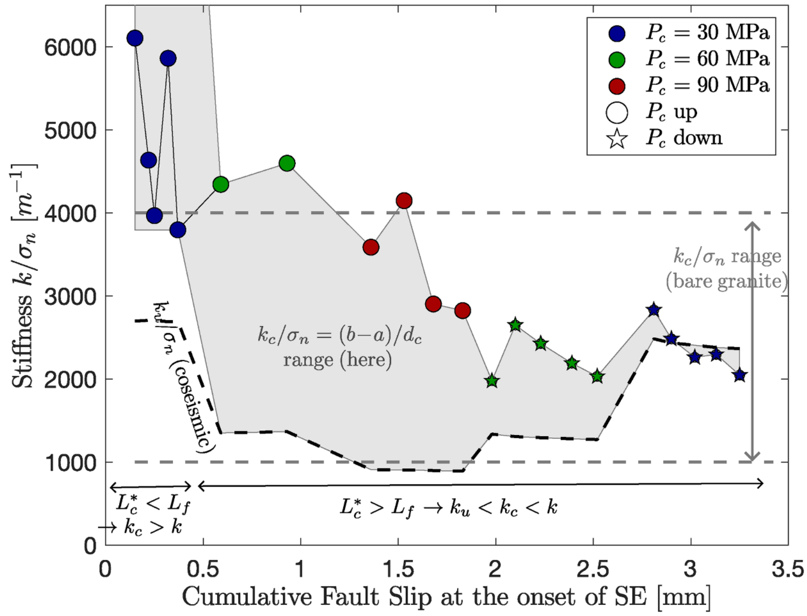

Fig. 6. Stiffness $k = -\partial\tau/\partial\delta$ computed from macroscopic strain gauges data (colored symbols) vs. cumulative slip at the onset SEs. The black solid line indicates unloading stiffness k_u estimated during the coseismic unloading (Figure S2). Gray dashed lines indicate the range of critical stiffness $k_c/\sigma_n = (b-a)/d_c$ (assuming rate-and-state friction) expected for bare granite surfaces from previous experiments reported in the literature. The gray shaded area indicates the range of $(b-a)/d_c$ needed to explain the occurrence of SE in our experiment, and its evolution with cumulative slip. Black arrows indicate the slip range where nucleation patch does not expand to the fault boundaries ($L_c^* < L_f$), and the slip range where the nucleation patch reaches the fault boundaries ($L_c^* > L_f$).

the stiffness became lower than k_c during the nucleation, either during k evolution, or when dropping to k_u. In the first case, having $k = k_c$ is consistent with having $R_{nuc} = L_c^* < L_f$. In the second case, the instability is driven by k_u that does not depend on a slipping patch size, and remains smaller than k_c. Thus, unstable slip is possible even if the theoretical $L_c^* > L_f$. We show in the next section that the observation of unstable slip in our experiments has strong implications concerning the evolution of k_c/σ_n.

4. Discussion

Using a kinematic inversion method, we were able to image the spatio-temporal evolution of preslip during the nucleation of 21 stick-slip events on the same experimental fault, under 3 different levels of confining pressures P_c. The Bayesian framework used allowed to estimate the corresponding uncertainties, essentially related to the gauge network that can only monitor axial strain on the external ream of the fault, as discussed in details by Dublanchet et al. (2024). The mesh used for the inversion is also optimized to get the best resolution while keeping a tractable number of parameters to infer (Dublanchet et al., 2024). Nevertheless our method could reveal a clear evolution of the preslip pattern (preslip duration, expansion rate, final slip, nucleation length) with cumulative slip along the fault accross successive SEs. This evolution is asymmetric and irreversible with respect to changes in confining pressure, suggesting that a non-recoverable mechanical evolution of the interface over successive SEs occurs on top of elastic stress effects.

The increase in L_c^*, for instance, could be related to progressive changes in the frictional properties of the interface as successive SEs accumulate slip on the fault, consistent with the evolution of the effective static friction coefficient f_0 shown in Figure S1. Note that Wang and Dresen (2025) also report L_c values that deviate from a simple inverse scaling with normal stress for saw-cut sandstone samples tested under triaxial conditions. Based on acoustic emission statistics and microstructural observations, Wang and Dresen (2025) interpret this deviation as resulting from enhanced damage accumulation and compaction with fault slip, leading to higher critical slip distances d_c. Because both damage and compaction intensify with increasing normal stress, this mechanism could counteract the expected reduction of L_c^* with stress. A similar interpretation was proposed by Paglialunga et al. (2022), who reported a linear increase of d_c with normal stress during dynamic rupture experiments.

Under rate-and-state friction, the increase in nucleation length could further be attributed to the evolution of the frictional parameters a, b, and d_c. Our results allow to estimate the evolution of $(a-b)/d_c$ of our experimental fault, as illustrated in Fig. 6. For small cumulative slip (first events at 30 MPa confining pressure), we know from preslip imaging that instability starts before slip fronts reach the fault boundaries ($L_c^* < L_f$), thus the normalized stiffness values k/σ_n obtained during nucleation provides a lower bound on $k_c/\sigma_n = (b-a)/d_c$, of the order of 4000 m^{-1}. For larger cumulative slip, preslip fronts reach the fault boundaries before unstable slip occurs ($L_c^* > L_f$), meaning that k_c should lie between k and k_u. The gray shaded area in Fig. 6 indicates the range of possible $k_c/\sigma_n = (b-a)/d_c$ that would explain our results. We thus conclude that $(b-a)/d_c$ should decrease by a factor of 3 for 3 mm of cumulative slip. The range of $(b-a)/d_c$ reported here is consistent with previous estimates for bare granite surfaces (Biegel et al., 1989; Marone et al., 1992; Beeler et al., 1996; Harbord et al., 2017) where $0.004 > b-a > 0.002$, $d_c \simeq 1-2\mu m$ (gray dashed lines in Fig. 6). Systematic changes in $a-b$ and d_c with cumulative slip have been measured for quartz-rich faults, both in bare and gouge-bearing configurations, as well as for gouge layers sheared in biaxial and rotary setups under moderate normal stress (Biegel et al., 1989; Marone and Kilgore, 1993; Beeler et al., 1996; Mair and Marone, 1999; Hadizadeh et al., 2015; Leeman et al., 2016; Scuderi et al., 2017b; Bedford and Faulkner, 2021; Bedford et al., 2022; Noël et al., 2023, 2024; Arts et al., 2024). Under such conditions, $a-b$ and d_c typically evolve within the first 10–20 mm of slip, which exceeds the total cumulative offset in our experiments. In this framework, the decrease in $(b-a)/d_c$ observed here could be interpreted as an increase in d_c at constant $b-a$ due to wear accumulation over successive SE, leading to the growth of a gouge layer. Following Marone and Kilgore (1993), an increase of d_c from $1\mu m$ to $3\mu m$ could be explained by such a process, with a final shear sone thickness of the order of 0.2 mm. In addition, the observed increase in peak fault strength with cumulative slip and confining pressure may also result from partial melting of asperities during dynamic rupture, which can locally weld and strengthen the fault interface (Passelègue et al., 2016; Lockner et al., 2017; Aubry et al., 2018). Such transient melting and subsequent solidification of contact junctions could increase interface cohesion, increase d_c, thereby influencing the apparent scaling of L_c^* with normal stress. The increase of critical nucleation length is also consistent with a stabilization of the nucleation process, with smaller expansion speed, and larger nucleation duration (Fig. 5a and c) as net slip accumulates on the fault.

However, the apparatus used does not allow to perform velocity step test (Leeman et al., 2016) under controlled conditions preventing us from a measurement of $a - b$ and d_c (and thus k_c/σ_n) so as to support our interpretation. Nevertheless, alternative estimates of postseismic changes in frictional parameters have recently been obtained in a similar triaxial stick-slip experiment using a bimaterial specimen (Noël et al., 2025).

The nucleation features reported in Figs. 3–5 were determined using a threshold of 2 μm of cumulative slip, which corresponds to 20 to 50 % of the mean slip accumulated on the fault at the onset of SEs (Fig. 1b). To estimate to what extent the results reported depend on this threshold, we performed the same analysis using a slip threshold of 1 μm. We also considered two cases where the pre-slip zone is defined with a slip-rate threshold of 0.1 and 0.4 μm.s^{-1}. The results are shown in Figures S66 to S74 of the supplementary material. Overall, our conclusions concerning the expansion rates, the nucleation duration, the maximum slip rate over successive reactivation are not affected by the threshold chosen. Concerning the critical nucleation length, we still get a non reversible evolution over successive SEs, where L_c^* does not follow the pure inverse normal stress scaling, but the trend strongly depends on the threshold. Using a slip-rate threshold, L_c^* are smaller than when a slip threshold is used. Note that many L_c^* values are close to the fault length. Considering the large uncertainty on L_c^* caused by the resolution of the method, but also by the complex shape of the nucleation patch, we could only conclude that L_c^* is of the same order of magnitude than the fault length. Thus the nucleation process is likely frustrated, in the sense that nucleation patch does not develop to its final size.

The results presented here (in particular for the critical nucleation length L_c^*) for a series of SEs confirm our previous interpretation (Dublanchet et al., 2024) that with our triaxial setup, we observe two types of nucleation process. In the first case instability is dictated by Linear Elastic Fracture Mechanics (LEFM) (Lawn, 1993) and reaching a critical nucleation length, smaller than the total fault length. In the second, instability is dictated by friction and by the release of elastic energy stored in the column through rigid block motion that interrupted the LEFM process when preslip fronts reached the fault limits. We call the second kind of instability a frustrated nucleation in the sense it involves an interrupted or frustrated preslip phase, that suddenly transitions to rigid block instability. Note that this behavior had already been described by Mclaskey and Yamashita (2017). We thus provide here additional evidence to this frustrated nucleation model.

According to the conceptual model of nucleation derived from previous experiments (Ohnaka and Shen, 1999; Nielsen et al., 2010; Latour et al., 2013), we only resolve here the quasi-static stage of nucleation, where expansion rate remains approximately constant, or eventually decreases as the nucleation patch approaches the fault boundaries (Fig. 4c). Expansion rates $\dot{S}_{nuc}$ ranging from 10 to 50 m^2.day^{-1} as observed would correspond to V_r between 40 and 200 m.day^{-1} according to the simple scaling of Eq. (1), in the lower range of quasi-static propagation speeds observed during previous nucleation experiments (Latour et al., 2013; Mclaskey and Yamashita, 2017; Selvadurai et al., 2017; Guérin-Marthe et al., 2019b; McLaskey, 2019; Cebry et al., 2022). Similarly, the slip rates involved during pre-slip (between 0.1 and 20 μm.s^1) typically correspond to the quasi-static range.

Interestingly, we do not capture an acceleration of the expansion towards dynamic rupture, but a slight deceleration of the expansion, which deviates from the classical conceptual model of Ohnaka and Shen (1999), Nielsen et al. (2010), Latour et al. (2013). We suspect this could be a consequence of particular stress conditions related to the small finite size of the fault, or to differences in material (Westerly Granite vs. PMMA) and loading rate, both being features affecting the nucleation process (Guérin-Marthe et al., 2019a). The gradual decrease of expansion rate before macroscopic failure could also suggest that part of the stored elastic energy is dissipated through distributed inelastic deformation or microcrack damage within the fault zone, which reduces the stress concentration at the rupture front. Such effects have been observed in other triaxial stick-slip experiments conducted under comparable conditions (Dresen et al., 2020; Wang and Dresen, 2025) and are consistent with the limited acceleration observed here. Finite size effects during the nucleation of dynamic ruptures can play a significant role as recently demonstrated by Gvirtzman et al. (2025). This issue requires further investigation, either with new experiments at a different scale, or using numerical modeling of the fault response.

An important implication of our conclusions regarding the frustrated nucleation concerns the amount of quasi-static aseismic pre-slip moment released by the fault during the nucleation phase. In a perspective of earthquake hazard assessment, it is important to analyze how this quantity scales with the coseimic moment released by the main slip event (SE) (Acosta et al., 2019; Wang and Dresen, 2025), the rate of acoustic emissions (Marty et al., 2023) or with material properties and loading. We show here that it can only be accurately estimated in case the nucleation is not frustrated, which requires first characterizing the whole spatio-temporal evolution of slip and the nucleation length.

5. Conclusion

Kinematic inversion of stick-slip events nucleation in a granite saw-cut sample under triaxial conditions reveals how the space-time evolution of quasi-static aseismic slip can change with the cumulative fault slip arising from repeated reactivation of the experimental fault. We relate this evolution to a change in frictional properties caused by dynamic slip events of the interface that may dominate over the confining stress effect. Our results illustrate well a frustrated nucleation process on a subcritical fault: an aseismic slip event first grows quasi-statically and instantaneously becomes unstable once it reaches the fault boundaries, before reaching its unstable size. The instability is then driven by friction and the effective stiffness of the sample and apparatus assembly, that remains low enough so that rigid block stick-slip events occur. We thus provide new physical insights into the very early initiation of slip under seismogenic stress conditions, but also propose a new way of interpreting triaxial experiments dedicated to earthquake nucleation.

Open research

To ensure full reproducibility and ease-of-use of our framework, we provide the data used to perform the inversions at Dublanchet et al. (2025). The MATLAB modules (KISLAB) used for the inversion are accessible at https://github.com/Pierre-Dublanchet/kislab/releases Dublanchet (2024).

CRediT authorship contribution statement

P. Dublanchet: Writing – original draft, Validation, Software, Methodology, Investigation, Formal analysis, Data curation, Conceptualization; **F.X. Passelégue:** Writing – original draft, Methodology, Investigation, Funding acquisition, Formal analysis, Data curation, Conceptualization; **H. Chauris:** Writing – review & editing, Validation, Investigation, Formal analysis; **A. Gesret:** Writing – review & editing, Validation, Methodology, Investigation, Formal analysis; **C. Noël:** Writing – review & editing, Formal analysis, Data curation.

Data availability

data and code available (links in the manuscript)

Declaration of competing interests

The authors declare the following financial interests/personal relationships which may be considered as potential competing interests:

F.X. Passelegue reports financial support was provided by European Commission. If there are other authors, they declare that they have no known competing financial interests or personal relationships that could have appeared to influence the work reported in this paper.

Acknowledgments

The authors thank C. Twardzik for insightfull discussions about the study. F.X.P acknowledges funding from the European Union (ERC Starting Grant HOPE num. 101041966).

Supplementary material

Supplementary material associated with this article can be found in the online version at 10.1016/j.epsl.2026.120060.

References

Acosta, M., Passelègue, F.X., Schubnel, A., Madariaga, R., Violay, M., 2019. Can precursory moment release scale with earthquake magnitude? A view from the laboratory. Geophys. Res. Lett. 46 (22), 12927–12937.
Arts, J. P.B., Niemeijer, A.R., Drury, M.R., Willingshofer, E., Matenco, L.C., 2024. The frictional strength and stability of spatially heterogeneous fault gouges. Earth Planet. Sci. Lett. 628, 118586. https://doi.org/10.1016/j.epsl.2024.118586
Aubry, J., Passelègue, F.X., Deldicque, D., Girault, F., Marty, S., Lahfid, A., Bhat, H.S., Escartin, J., Schubnel, A., 2018. Frictional heating processes and energy budget during laboratory earthquakes. Geophys. Res. Lett. 45 (22), 12–274.
Bedford, J.D., Faulkner, D.R., 2021. The role of grain size and effective normal stress on localization and the frictional stability of simulated quartz gouge. Geophys. Res. Lett. 48 (7), e2020GL092023. https://doi.org/10.1029/2020GL092023
Bedford, J.D., Faulkner, D.R., Lapusta, N., 2022. Fault rock heterogeneity can produce fault weakness and reduce fault stability. Nat. Commun. 13 (1), 326.
Beeler, N.M., Tullis, T.E., Blanpied, M.L., Weeks, J.D., 1996. Frictional behavior of large displacement experimental faults. J. Geophys. Res. Solid Earth 101 (B4), 8697–8715.
Biegel, R.L., Sammis, C.G., Dieterich, J.H., 1989. The frictional properties of a simulated gouge having a fractal particle distribution. J. Struct. Geol. 11 (7), 827–846.
Blanpied, M.L., Marone, C.J., Lockner, D.A., Byerlee, J.D., King, D.P., 1998. Quantitative measure of the variation in fault rheology due to fluid-rock interactions. J. Geophys. Res. Solid Earth 103 (B5), 9691–9712.
Bletery, Q., Nocquet, J.-M., 2023. The precursory phase of large earthquakes. Science 381 (6655), 297–301.
Bouchon, M., Durand, V., Marsan, D., Karabulut, H., Schmittbuhl, J., 2013. The long precursory phase of most large interplate earthquakes. Nat. Geosci. 6 (4), 299–302.
Broyden, C.G., 1970. The convergence of a class of double-rank minimization algorithms: 2. The new algorithm. IMA J. Appl. Math. 6 (3), 222–231.
Cabrera, L., Poli, P., Frank, W.B., 2022. Tracking the spatio-temporal evolution of foreshocks preceding the Mw 6.1 2009 L'aquila earthquake. J. Geophys. Res. Solid Earth 127 (3), e2021JB023888.
Campillo, M., Ionescu, I.R., 1997. Initiation of antiplane shear instability under slip dependent friction. J. Geophys. Res. Solid Earth 102 (B9), 20363–20371.
Cebry, S. B.L., Ke, C.-Y., Shreedharan, S., Marone, C., Kammer, D.S., McLaskey, G.C., 2022. Creep fronts and complexity in laboratory earthquake sequences illuminate delayed earthquake triggering. Nat. Commun. 13 (1), 6839.
Chambon, G., Rudnicki, J.W., 2001. Effects of normal stress variations on frictional stability of a fluid-infiltrated fault. J. Geophys. Res. Solid Earth 106 (B6), 11353–11372.
Chayes, F., 1950. Composition of the granites of westerly and bradford, rhode island. Am. J. Sci. 248 (6), 378–407.
Dieterich, J.H., 1978. Preseismic fault slip and earthquake prediction. J. Geophys. Res. Solid Earth 83 (B8), 3940–3948.
Dieterich, J.H., 1981. Constitutive properties of faults with simulated gouge. Mech. Behav. Crustal Rocks: Handin Vol. 24, 103–120.
Dieterich, J.H., Linker, M.F., 1992. Fault stability under conditions of variable normal stress. Geophys. Res. Lett. 19 (16), 1691–1694.
Dodge, D.A., Beroza, G.C., Ellsworth, W.L., 1996. Detailed observations of California foreshock sequences: implications for the earthquake initiation process. J. Geophys. Res. Solid Earth 101 (B10), 22371–22392.
Dresen, G., Kwiatek, G., Goebel, T., Ben-Zion, Y., 2020. Seismic and aseismic preparatory processes before large stick–slip failure. Pure Appl. Geophys. 177, 5741–5760.
Dublanchet, P., Passelègue, F.X., Chauris, H., Gesret, A., Twardzik, C., Nöel, C., 2024. Kinematic inversion of aseismic fault slip during the nucleation of laboratory earthquakes. J. Geophys. Res. Solid Earth 129 (12), e2024JB028733.
Dublanchet P., Passelégue F.X., Chauris H., Gesret A., Twardzik C., Noël C., 2025 Strain and slip data for kinematic inversion of fault slip during the nucleation of laboratory earthquakes https://doi.org/10.5281/zenodo.15606648.
Dublanchet P., 2024 Pierre-dublanchet/kislab: first release https://doi.org/10.5281/zenodo.13948072.
Fletcher, R., 1970. A new approach to variable metric algorithms. Comput. J. 13 (3), 317–322.
Fryer, B., Giorgetti, C., Passelègue, F., Momeni, S., Lecampion, B., Violay, M., 2022. The influence of roughness on experimental fault mechanical behavior and associated microseismicity. J. Geophys. Res. Solid Earth 127 (8), e2022JB025113.
Giorgetti, C., Violay, M., 2021. The influence of loading path on fault reactivation: a laboratory perspective. Geophys. Res. Lett. 48 (8), e2020GL091466.
Goldfarb, D., 1970. A family of variable-metric methods derived by variational means. Math. Comput. 24 (109), 23–26.
Guérin-Marthe, S., Kwiatek, G., Wang, L., Bonnelye, A., Martínez-Garzón, P., Dresen, G., 2023. Preparatory slip in laboratory faults: effects of roughness and load point velocity. J. Geophys. Res. Solid Earth 128 (4), e2022JB025511.
Guérin-Marthe, S., Nielsen, S., Bird, R., Giani, S., Di Toro, G., 2019a. Earthquake nucleation size: evidence of loading rate dependence in laboratory faults. J. Geophys. Res. Solid Earth 124 (1), 689–708.
Guérin-Marthe, S., Nielsen, S., Bird, R., Giani, S., Di Toro, G., 2019b. Earthquake nucleation size: evidence of loading rate dependence in laboratory faults. J. Geophys. Res. Solid Earth 124 (1), 689–708.
Gvirtzman, S., Fineberg, J., 2021. Nucleation fronts ignite the interface rupture that initiates frictional motion. Nat. Phys. 17 (9), 1037–1042.
Gvirtzman, S., Kammer, D.S., Adda-Bedia, M., Fineberg, J., 2025. How frictional ruptures and earthquakes nucleate and evolve. Nature 637 (8045), 369–374.
Hadizadeh, J., Tullis, T.E., White, J.C., Konkachbaev, A.I., 2015. Shear localization, velocity weakening behavior, and development of cataclastic foliation in experimental granite gouge. J. Struct. Geol. 71, 86–99.
Harbord, C. W.A., Nielsen, S.B., De Paola, N., Holdsworth, R.E., 2017. Earthquake nucleation on rough faults. Geology 45 (10), 931–934.
Hastings, W.K., 1970. Monte carlo sampling methods using markov chains and their applications Oxford University Press.
He, C., Ma, S., Huang, J., 1998. Transition between stable sliding and stick-slip due to variation in slip rate under variable normal stress condition. Geophys. Res. Lett. 25 (17), 3235–3238.
Kato, N., Yamamoto, K., Yamamoto, H., Hirasawa, T., 1992. Strain-rate effect on frictional strength and the slip nucleation process. Tectonophysics 211 (1–4), 269–282.
Latour, S., Schubnel, A., Nielsen, S., Madariaga, R., Vinciguerra, S., 2013. Characterization of nucleation during laboratory earthquakes. Geophys. Res. Lett. 40 (19), 5064–5069.
Lawn, B., 1993. Fracture of brittle solids. Camb. Solid State Sci. Ser., 2 , 307–334.
Leeman, J.R., Marone, C., Saffer, D.M., 2018. Frictional mechanics of slow earthquakes. J. Geophys. Res. Solid Earth 123 (9), 7931–7949.
Leeman, J.R., Saffer, D.M., Scuderi, M.M., Marone, C., 2016. Laboratory observations of slow earthquakes and the spectrum of tectonic fault slip modes. Nat. Commun. 7 (1), 11104.
Lockner, D.A., Kilgore, B.D., Beeler, N.M., Moore, D.E., 2017. The transition from frictional sliding to shear melting in laboratory stick-slip experiments. Fault Zone Dyn. Process. Evol. Fault Prop. Dur. Seism. Rupture , 6, 103–131.
Mair, K., Marone, C., 1999. Friction of simulated fault gouge for a wide range of velocities and normal stresses. J. Geophys. Res. Solid Earth 104 (B12), 28899–28914.
Marone, C., 1998. The effect of loading rate on static friction and the rate of fault healing during the earthquake cycle. Nature 391 (6662), 69–72.
Marone, C., Hobbs, B.E., Ord, A., 1992. Coulomb constitutive laws for friction: contrasts in frictional behavior for distributed and localized shear. Pure Appl. Geophys. 139 (2), 195–214.
Marone, C., Kilgore, B., 1993. Scaling of the critical slip distance for seismic faulting with shear strain in fault zones. Nature 362 (6421), 618–621.
Marone, C., Raleigh, C.B., Scholz, C.H., 1990. Frictional behavior and constitutive modeling of simulated fault gouge. J. Geophys. Res. Solid Earth 95 (B5), 7007–7025.
Marty, S., Schubnel, A., Bhat, H.S., Aubry, J., Fukuyama, E., Latour, S., Nielsen, S., Madariaga, R., 2023. Nucleation of laboratory earthquakes: quantitative analysis and scalings. J. Geophys. Res. Solid Earth 128 (3), e2022JB026294.
McLaskey, G.C., 2019. Earthquake initiation from laboratory observations and implications for foreshocks. J. Geophys. Res. Solid Earth 124 (12), 12882–12904.
McLaskey, G.C., Kilgore, B.D., 2013. Foreshocks during the nucleation of stick-slip instability. J. Geophys. Res. Solid Earth 118 (6), 2982–2997.
McLaskey, G.C., Lockner, D.A., 2014. Preslip and cascade processes initiating laboratory stick slip. J. Geophys. Res. Solid Earth 119 (8), 6323–6336.
Mclaskey, G.C., Yamashita, F., 2017. Slow and fast ruptures on a laboratory fault controlled by loading characteristics. J. Geophys. Res. Solid Earth 122 (5), 3719–3738.
Metropolis, N., Rosenbluth, A.W., Rosenbluth, M.N., Teller, A.H., Teller, E., 1953. Equation of state calculations by fast computing machines. J. Chem. Phys. 21 (6), 1087–1092.
Nagao, T., Orihara, Y., Kamogawa, M., 2014. Precursory phenomena possibly related to the 2011 m9. 0 off the pacific coast of Tohoku earthquake. J. Disaster Res. 9 (3), 303–310.
Nielsen, S., Taddeucci, J., Vinciguerra, S., 2010. Experimental observation of stick-slip instability fronts. Geophys. J. Int. 180 (2), 697–702.
Noël, C., Giorgetti, C., Collettini, C., Marone, C., 2024. The effect of shear strain and shear localization on fault healing. Geophys. J. Int. 236 (3), 1206–1215.
Noël, C., Giorgetti, C., Scuderi, M.M., Collettini, C., Marone, C., 2023. The effect of shear displacement and wear on fault stability: laboratory constraints. J. Geophys. Res. Solid Earth 128 (4), e2022JB026191.

Noël, C., Passelègue, F.X., Giorgetti, C., Violay, M., 2019. Fault reactivation during fluid pressure oscillations: transition from stable to unstable slip. J. Geophys. Res. Solid Earth 124 (11), 10940–10953.

Noël, C., Twardzik, C., Dublanchet, P., Passelègue, F., 2025. On the emergence of fault afterslip during laboratory seismic cycles. Earth Planet. Sci. Lett. 658, 119288.

Ohnaka, M., Shen, L.-f., 1999. Scaling of the shear rupture process from nucleation to dynamic propagation: implications of geometric irregularity of the rupturing surfaces. J. Geophys. Res. Solid Earth 104 (B1), 817–844.

Paglialunga, F., Passelègue, F.X., Brantut, N., Barras, F., Lebihain, M., Violay, M., 2022. On the scale dependence in the dynamics of frictional rupture: constant fracture energy versus size-dependent breakdown work. Earth Planet. Sci. Lett. 584, 117442.

Passelègue, F.X., Latour, S., Schubnel, A., Nielsen, S., Bhat, H.S., Madariaga, R., 2017. Influence of fault strength on precursory processes during laboratory earthquakes. Fault Zone Dyn. Process. Evol. Fault Prop. Dur. Seism. Rupture , 12, 229–242.

Passelègue, F.X., Schubnel, A., Nielsen, S., Bhat, H.S., Deldicque, D., Madariaga, R., 2016. Dynamic rupture processes inferred from laboratory microearthquakes. J. Geophys. Res. Solid Earth 121 (6), 4343–4365.

Pozzi, G., Scuderi, M.M., Tinti, E., Nazzari, M., Collettini, C., 2022. The role of fault rock fabric in the dynamics of laboratory faults. J. Geophys. Res. Solid Earth 127 (6), e2021JB023779.

Rathbun, A.P., Marone, C., 2010. Effect of strain localization on frictional behavior of sheared granular materials. J. Geophys. Res. Solid Earth 115 (B1).

Richardson, E., Marone, C., 1999. Effects of normal stress vibrations on frictional healing. J. Geophys. Res. Solid Earth 104 (B12), 28859–28878.

Roeloffs, E.A., 2006. Evidence for aseismic deformation rate changes prior to earthquakes. Annu. Rev. Earth Planet. Sci. 34 (1), 591–627.

Rubin, A.M., Ampuero, J.-P., 2005. Earthquake nucleation on (aging) rate and state faults. J. Geophys. Res. Solid Earth 110 (B11).

Ruiz, S., Metois, M., Fuenzalida, A., Ruiz, J., Leyton, F., Grandin, R., Vigny, C., Madariaga, R., Campos, J., 2014. Intense foreshocks and a slow slip event preceded the 2014 iquique m w 8.1 earthquake. Science 345 (6201), 1165–1169.

Scuderi, M.M., Collettini, C., Marone, C., 2017a. Frictional stability and earthquake triggering during fluid pressure stimulation of an experimental fault. Earth Planet. Sci. Lett. 477, 84–96.

Scuderi, M.M., Collettini, C., Viti, C., Tinti, E., Marone, C., 2017b. Evolution of shear fabric in granular fault gouge from stable sliding to stick slip and implications for fault slip mode. Geology 45 (8), 731–734.

Selvadurai, P.A., Glaser, S.D., 2017. Asperity generation and its relationship to seismicity on a planar fault: a laboratory simulation. Geophys. J. Int. 208 (2), 1009–1025.

Selvadurai, P.A., Glaser, S.D., Parker, J.M., 2017. On factors controlling precursor slip fronts in the laboratory and their relation to slow slip events in nature. Geophys. Res. Lett. 44 (6), 2743–2754.

Shanno, D.F., 1970. Conditioning of quasi-newton methods for function minimization. Math. Comput. 24 (111), 647–656.

Shreedharan, S., Bolton, D.C., Rivière, J., Marone, C., 2020. Preseismic fault creep and elastic wave amplitude precursors scale with lab earthquake magnitude for the continuum of tectonic failure modes. Geophys. Res. Lett. 47 (8), e2020GL086986.

Uchida, N., Matsuzawa, T., 2013. Pre-and postseismic slow slip surrounding the 2011 Tohoku-oki earthquake rupture. Earth Planet. Sci. Lett. 374, 81–91.

Uenishi, K., Rice, J.R., 2003. Universal nucleation length for slip-weakening rupture instability under nonuniform fault loading. J. Geophys. Res. Solid Earth 108 (B1).

Wang, L., Dresen, G., 2025. Premonitory slip, rupture propagation, and frictional sliding on laboratory faults in porous sandstone: effects of loading rate and confining pressure. J. Geophys. Res. Solid Earth 130 (5), e2025JB031463.

Xu, S., Fukuyama, E., Yamashita, F., Mizoguchi, K., Takizawa, S., Kawakata, H., 2018. Strain rate effect on fault slip and rupture evolution: insight from meter-scale rock friction experiments. Tectonophysics 733, 209–231.